Multi-spectral surface emissivity as an indicator of soil water content and soil water content changes in arid soils

D. Kool [a], N. Agam [b],[*]

[a] *Dept. of Environmental, Geoinformatic, and Urban Planning Sciences, Ben-Gurion University of the Negev, Be'er Sheva 8499000, Israel*
[b] *Jacob Blaustein Institutes for Desert Research, Ben-Gurion University of the Negev, Sede Boqer Campus, Be'er Sheva 8499000, Israel*

ARTICLE INFO

ABSTRACT

Surface emissivity (ε) is used to characterize surfaces and to determine surface temperature from thermal radiation data. While in many applications it is treated as a constant, it is known to change with surface water content. Several ASTER/SEVERI based studies have speculated that diurnal changes in ε over deserts are linked to diurnal soil water content cycles resulting from water vapor adsorption during the night and subsequent evaporation during the day. This paper aims, for the first time, to validate the relationship between diurnal changes in surface ε and the changes in soil water content due to water vapor adsorption and evaporation under natural conditions. Measurements were conducted with a 6-band infrared radiometer, designed to validate ASTER bands 10–14, with study-specific recalibration for improved accuracy of ε. The evaluation included two different approaches to determine ε: using a single reference band (1B) and using the temperature/emissivity separation algorithm (TES) . water content. While the TES has proven itself in many applications, it was found that for the soils studied (sand and loess) the use of 1B approach gave more consistent results for ε changes with soil water content than TES. Emissivity could be a powerful tool to characterize little studied soil water content changes in arid regions, but will require better characterization of surface properties to quantify the relationship between ε and soil water content for various soil types. Additional challenges to upscale this method include properly accounting for air irradiance and spatial heterogeneity. Meeting these main challenges will lead the way to detect small changes in soil water content under dry conditions at larger scales. Whether these are a result of water vapor adsorption or other processes, detecting such small changes in soil water content will provide new insights into desert hydrology.

1. Introduction

Soil water content has been recognized as an essential climate variable in assessing climate change, both as a component of the global water balance and for its determining role in energy partitioning at the earth's surface (GCOS, 2011). As such, efforts to estimate soil water content at a global scale have intensified in the last decade (Babaeian et al., 2019; Dorigo et al., 2015). Long-term projections of changes in the water cycle show particularly low model agreement for surface soil water content in desert areas (IPCC, 2021). Given that arid and hyper-arid regions comprise 27% of the terrestrial surface (Zomer et al., 2022), inaccurate estimation of surface water content in desert regions could be an important source of uncertainty in long-term water cycle projections and closure of the global energy budget (Agam et al., 2004a). In deserts, increases in soil water content occur during scarce and unpredictable rain events, and, on a more regular basis, as a result of non-rainfall water inputs (fog, dew, and water vapor adsorption). Most used approaches to assess soil water content were not designed to determine soil water content at the very low water content range observed in deserts, or to be sensitive to minute diurnal changes in water content associated with non-rainfall water inputs.

Global estimations of soil water content primarily rely on remotely sensed surface radiation data, from shortwave to thermal to microwave ranges within the electromagnetic spectrum. Microwave radiation can be related to the dielectric properties of soil, which are directly proportional to soil water content. The thickness of the soil layer represented by this measurement is larger for drier soils. Water content measured in the L-band, for example, was found to represent an average of the top 5–18 cm soil layer for water contents in the range 0.1–0.4 cm^3/cm^3, and of the top 18–70 cm layer at lower water contents (<0.1

---

cm^3/cm^3) (Lv et al., 2018). The reported root mean square errors of soil water content obtained from different microwave methods generally range between 0.02 and 0.08 cm^3 cm^{-3} (Hu et al., 2023; Ochsner et al., 2013; Zhao et al., 2021). Unlike thermal and optical range radiation, microwave radiation can penetrate clouds and vegetation allowing soil water content content measurement under a large range of conditions (Babaeian et al., 2019; Brocca et al., 2017; Ochsner et al., 2013; Petropoulos et al., 2015). Given the lack of vegetation or cloud-cover in arid regions, microwave-based approaches are not necessarily the best option to determine soil water content there, particularly since thermal and optical range imagery is generally available at higher spatial resolutions.

Thermal radiation is a function of the surface temperature and emissivity, and generally soil water content is derived from surface temperature using either thermal inertia or energy balance approaches. Thermal inertia approaches derive soil water content using the principle that since water has a higher capacity than dry soil, the diurnal fluctuation in surface temperature decreases with increasing soil water content (Maltese et al., 2013; Verstraeten et al., 2006). Alternatively, given that available water drives energy partitioning between latent and sensible heat fluxes, and that surface temperature is determined by the energy balance at the soil surface, one can use surface temperature to solve for soil water content using energy balance-based approaches (Babaeian et al., 2019). In the optical range, soil water content is derived by comparing reflection by wavebands that are strongly absorbed by water to wavebands that are less sensitive to water. This method is, however, sensitive to atmospheric water vapor and to surface properties (Babaeian et al., 2019; Petropoulos et al., 2015). The reported accuracy of soil water content obtained using any of these methods is about ± 0.04 cm^3 cm^{-3}, sometimes reaching as low as ± 0.03 cm^3 cm^{-3} or as high as ± 0.1 cm^3 cm^{-3} (Babaeian et al., 2019).

Accuracies reported for both microwave and thermal methods might be acceptable in humid environments, but are problematic in arid regions. In loess soils in the Negev desert, non-rainfall water inputs amount to 0.3–0.4 mm per night during the summer months (Agam and Berliner, 2004; Florentin and Agam, 2017). In the sandy Namib desert, data collected in February, September, and October, indicate consistent non-rainfall water inputs amounting to 0.1–0.2 mm per night (Kool et al., 2021; Spirig et al., 2019). In both, water content changes occur primarily in the top 1–2 cm soil layer, with minor changes observed up to a depth of 5 cm. Associated soil surface water content ranged from 0.01 to 0.03 cm^3 cm^{-3} in loess (Agam and Berliner, 2004), and 0.002 to 0.02 cm^3 cm^{-3} in sand (Kool et al., 2021). In both the Negev and the Namib deserts, water vapor adsorption was the primary form of non-rainfall water inputs. The conditions required for each type of non-rainfall water input are slightly different: when the air or the surface temperature drops below dewpoint temperature, the result is fog or dew, respectively, while water vapor adsorption occurs when the humidity in the soil drops below the humidity of the air. Since water vapor adsorption does not have temperature requirements it is likely the most ubiquitous form of non-rainfall water inputs, albeit the smallest. To better understand the large-scale importance of water vapor adsorption in deserts there is a need for a monitoring approach that can accurately observe soil water content changes in the range of 0.002 to 0.03 cm^3 cm^{-3}. Given the shallow nature of the water vapor adsorption process, thermal infrared methods are more suitable to detect associated changes in soil water content than microwave-based methods.

Several studies have suggested using surface emissivity rather than surface temperature to determine soil water content from measurements in the thermal range (Mira, 2007; Salisbury and D'Aria, 1992; Wang et al., 2015). The temperature/emissivity separation (TES) algorithm (Gillespie et al., 1998, 2011; Schmugge et al., 1998), specifically developed for NASA's Advanced Spaceborne Thermal Emission and Reflection Radiometer (ASTER), is typically used to obtain both surface temperature and emissivity. Surface emissivity is known to increase with water content, but was found to affect band 10 (8.3 μm) more strongly

than the band 14 (11.35 μm), particularly in the airdry (0.03–0.07 g g^{-1}) water content range (Salisbury and D'Aria, 1992), with coarser soils showing a stronger response than lighter textured soils. Later studies confirmed a relatively steep linear increase in emissivity for the 8.3–9.3 μm band at lower water contents (<0.1 g g^{-1}) (Mira, 2007; Mira et al., 2010; Wang et al., 2015), indicating this method may be particularly relevant to arid regions.

Given the particular sensitivity of emissivity to water content at the dry end, a number of studies have already speculated that observed diurnal variations in emissivity in deserts may be linked to non-rainfall water inputs. A recent study in a dune field in California attributed a 0.04 night-time increase in ASTER-retrieved emissivity to water vapor adsorption (Mushkin et al., 2020). Studies using images from the geostationary Spinning Enhanced Visible and InfraRed Imager (SEVIRI) likewise reported strong diurnal dynamics in emissivity over deserts, especially in the 8.7 μm channel for both sandy and finer-textured soils (Li et al., 2012; Masiello et al., 2013, 2014; Rozenstein et al., 2015). These observations were assumed to be related to the diurnal soil water content cycle resulting from water vapor adsorption by the soil throughout the late afternoon and night and the subsequent evaporation in the morning (Masiello et al., 2014), but this relationship has never been validated. The objective of this paper was to substantiate the link between diurnal changes in surface emissivity and changes in soil water content due to water vapor adsorption and evaporation. Surface emissivity was determined using in-situ thermal infrared remote sensing measurement with high temporal and spectral (ASTER-like) resolution on several consecutive days. The radiometer was looking over undisturbed soil cores (both coarse and finer-textured) whose mass was concurrently monitored to determine changes in water content. This relationship exemplifies how infrared emissivity can replace radiative temperature to evaluate soil water content for specific applications.

2. Experimental design

2.1. Site description

Measurements were conducted at the Wadi Mashash Experimental Farm, in the Negev desert in Israel (31.07°N, 34.85°E; Fig. 1). Long-term minimum and maximum air temperature on site average between 5 °C and 15 °C in January and 19 °C and 32 °C in July. The mean long-term annual rainfall of 115 mm y^{-1} is restricted to the winter months. Similar to the surrounding desert, the site is characterized by a predominantly bare crusted soil surface and some scattered small shrubs. The loess soil is classified as a sandy loam Aridisol (Agam et al., 2004b). Long-term measurements on site include incoming and outgoing shortwave and longwave irradiance using a four-component net radiometer (SN500, Apogee Inc., Logan, UT) as well as temperature and relative humidity at 2 m height and wind speed at 10 m height as part of a standard meteorological station operated by the Israel Meteorological Service.

2.2. Lysimeter measurements

Over the summer (June–September) of 2021, daily accumulation and evaporation of water was measured using two weighing lysimeters, representing two contrasting soil types found in the region. The first lysimeter was obtained from an active dune crest (>94% sand) in the Nitzana area, 30.93°N, 34.41°E (Figs. 1, 2A). A disturbed sample rather than an undisturbed sample was extracted considering the lack of horizon development and absence of a surface crust. The second lysimeter was an undisturbed loess sample extracted from an area adjacent to the research site. The lysimeters consisted of 50 cm long PVC pipes with an internal diameter of 18.7 cm, which, after collecting the sample, were insulated with 2 cm thick polystyrene foam at the bottom and a ~ 4 cm spray foam layer wrapping the side. The lysimeters were placed flush with the soil surface, 70 m apart on automated scales (GP30KS, A & D, Tokyo, Japan). Additional Styrofoam insulation was placed around the
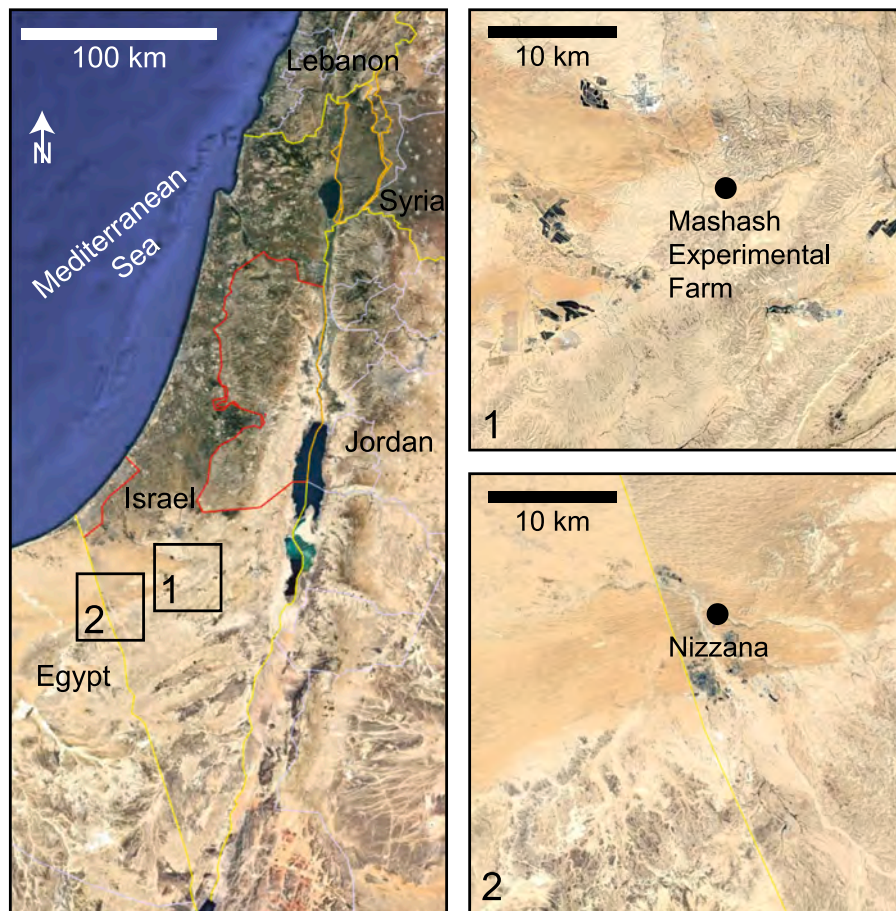
Fig. 1. Location of the Mashash Experimental Farm of the Blaustein Institutes for Desert Research, Ben-Gurion University where the experiment was conducted (31.07°N, 34.85°E), and the Nizzana sand dunes where the sand sample was collected (30.93°N, 34.41°E).

Fig. 2. Lysimeter preparation (A) and set-up (B) and radiometer deployment (C). The sand sample was filled by hand (A1–2), while the loess sample was an un-disturbed soil column (A3–4). After sealing the samples at the bottom, they were insulated with spray foam, and placed on a balance inside a pre-installed metal container, flush with the soil surface (B1). A Styrofoam block with a cylindrical opening for the lysimeter was mounted on ledges inside the metal container (B2). After covering the Styrofoam block with a thin layer of soil, the radiometer was attached to a moving arm next to the lysimeter, and set to move between the lysimeter (C1) and the reference standard (C2).

lysimeter and covered with a thin layer of soil as shown in Fig. 2B. Lysimeter mass was recorded every 5 s and stored as 15-min averages using a datalogger (CR310, Campbell Scientific, Logan, UT). Daily changes in mass as a result of accumulation and evaporation of water in the soil sample were observed at 0.1 g resolution, which is equivalent to 0.0036 mm water.

2.3. Radiometer measurements

Spectral radiance and brightness temperature were obtained using a 6-band (Table 1) infrared radiometer (CE312-N2, Cimel Electronique, Paris, France) developed specifically to provide on-ground verification of thermal infrared measurements in remotely sensed ASTER datasets (Brogniez et al., 2003; Legrand et al., 2000). The instrument has an accuracy of 0.1 °C, resolution of 0.01 °C, and can measure target temperatures between −80 °C and + 60 °C. The instrument was operated with company-provided software (Win RadioPda, Version 1.2) using a Windows-based tablet (Vanquisher SV-86H, Sinicvision Technology Co., Shenzen, China). A free macro software (Macro Toolworks, Pitrinec Software, Červený Kostelec, Czech Republic) allowed continuous measurements at defined time intervals. For simplicity, channels are referred to by their center wavelength (e.g., $i = 8.3$).

2.3.1. Configuration

Radiometer measurements can be configured using customizable scenarios. The default scenario starts with a head temperature measurement, followed by mirror and target measurements for individual band widths, with one full scenario taking about 40 s to complete. Using the provided calibration data, the software then calculates the radiance and brightness temperature for each bandwidth (Eqs. (5)–(7)).

In this study, the default scenario was found not accurate enough due to rapidly changing surface, air, and sensor head temperatures. This violated the assumption that temperatures remain relatively constant over the course of the 40 s measurement sequence. To account for changes in head temperature, the scenario was modified to include a head temperature measurement after each individual bandwidth measurement for a total of seven head temperature measurements per sequence. Furthermore, for the individual bandwidths, a mirror measurement was included both before and after a target measurement. This full sequence took 68 s to complete. During post-processing, radiance and brightness temperatures for each bandwidth were calculated using the target measurement and the average of the head temperature and mirror measurements obtained before and after each target measurement.

2.3.2. Calibration setup

The infrared radiometer was recalibrated to match the soil surface temperature range observed in the field, which has seasonal minima and maxima ranging from a little above 10 °C to almost 60 °C. The radiometer was set, facing down, on a portable blackbody calibration source (BB982, Calex Electronics Limited, Bedfordshire, UK) designed to calibrate infrared thermometers for the −20 °C to 125 °C temperature range. The blackbody has a 50 mm aperture diameter (150 mm deep) with a resolution of 0.01 °C, stability of 0.1 °C and emissivity >0.995. A platinum resistance thermometer provided the blackbody temperature

(T_{BB}) which was logged at 10 s intervals using the company software. Styrofoam was fitted around the radiometer head to provide insulation.

The calibration was conducted 14–20 June 2021 on the roof of the research institute, allowing the radiometer head to reach similar temperatures as it would under field conditions. The blackbody was programmed to maintain temperatures of 10 °C, 35 °C, and 60 °C for a minimum of 24 h per temperature. During calibration, the radiometer was set to perform three consecutive measurement sequences every 15 min, using the adapted measurement scenario described above. The calibration was evaluated over a 48-h validation period (18–20 July 2021), on the roof of the research institute, similar to the calibration set-up. For the validation period, the blackbody was programmed to change temperatures hourly, according to average hourly soil temperatures obtained from thermocouple measurements at 0.5 cm depth at the Mashash experimental station in July 2020.

2.3.3. Field deployment

Field measurements were conducted between 18 August and 23 September 2021, switching infrared radiometer measurements between the loess and sand samples. Data for the sand sample were collected from 29 August to 5 September and from 12 to 19 September, for a total of 14 nights. Technical issues and weather conditions limited data collection for the loess sample to a total of 11 nights spread over three weeks: 18–22 August, 26–29 August, and 19–23 September.

The radiometer (pointing downwards) was mounted on a 90 cm long aluminum arm which rotated on a solid metal pipe at a height of 50 cm (Fig. 2C). A counter-weight on the opposite end of the arm provided stability. The arm allowed movement of the radiometer between the lysimeter and a reference gold plate (25.4 × 25.4 cm, UIRT-94-100, Infragold diffuse reflectance standard, Labsphere, North Sutton, NH, USA) to obtain atmospheric reflectance ($L_{i\,sky}$;Eq. (10)). Gold plate kinetic temperature was measured using a thermocouple inserted at the back of the plate and insulated with aluminum foil and putty clay. The gold plate, of the same type as the one used by García-Santos et al. (2012) had a rough surface. The emissivity for all wavebands was set to 0.08 as measured by García-Santos et al. (2012).

A 5 V continuous rotation servomotor (FR5317M-FB, Feetech, Shenzhen, China) controlled by a CR1000 datalogger (Campbell Scientific Inc., Logan, UT, USA) ensured the arm moved to and maintained the desired position. Arm movement speed was set to 2° per second. The arm position (in degrees) was logged every 30 s. With a field of view of 10°, the area observed by the radiometer from 50 cm height had a diameter of about 9 cm, half of the lysimeter diameter. Assuming the radiometer was positioned perfectly above the lysimeter, the arm could move up to 4.5 cm or about 3° to either side without the radiometer losing full view of the lysimeter. Measurements for which the angle was off by >2°, due to, for example, strong winds, were discarded.

The base of the arm was set up on the north side of the lysimeter and the gold plate to avoid shading. Measurements were conducted at 15-min intervals, with a gold plate measurement both before and after each lysimeter measurement, coordinating the measurement time of the radiometer and the travel time of the arm (see example in Table 2).

3. Theory and methods

Radiance (L, Table 3) detected by the radiometer sensor ($L_{detected}$) is

Table 1
CE312 spectral bands.

Spectral bands		Center wavelength	Equivalent ASTER band #
8.0–14.0	μm	broad band (−)	–
8.1–8.5	μm	8.30 μm	10
8.5–8.9	μm	8.70 μm	11
8.9–9.3	μm	9.10 μm	12
10.3–11.0	μm	10.65 μm	13
11.0–11.7	μm	11.35 μm	14

Table 2
Example arm-radiometer coordination for a measurement at 12:00.

Active component	Position	Start	Finish
Radiometer	Gold plate	11:57:50	11:58:58
Arm	Moving towards lysimeter	11:59:00	11:59:45
Radiometer	Lysimeter	11:59:50	12:00:58
Arm	Moving towards gold plate	12:01:00	12:01:45
Radiometer	Gold plate	12:01:50	12:02:58

Table 3

List of abbreviations and symbols.

Definition	Term	Units
Single reference band approach	1B	
One of five sensor-specific empirical constants	a_i	(−)
Planck blackbody spectral radiance	B	mW cm^{-2} sr^{-1}
One of five sensor-specific empirical constants	b_i	(−)
Sensor detector output in digital counts	DC	(−)
One of five sensor-specific empirical constants	d_i	(−)
One of five sensor-specific empirical constants	e_i	(−)
Channel	i	(−)
Outgoing longwave irradiance	$I_{L\uparrow}$	W m^{-2}
Incoming longwave irradiance	$I_{L\downarrow}$	W m^{-2}
Outgoing shortwave irradiance	$I_{S\uparrow}$	W m^{-2}
Incoming shortwave irradiance	$I_{S\downarrow}$	W m^{-2}
Radiance	L	mW cm^{-2} sr^{-1} μm^{-1}
Air radiance (between sensor and target)	L_{air}	mW cm^{-2} sr^{-1} μm^{-1}
Radiometer-detected radiance	$L_{detected}$	mW cm^{-2} sr^{-1} μm^{-1}
Spectral radiance	L_i	mW cm^{-2} sr^{-1}
Sky-emitted spectral radiance	$L_{i\ sky}$	mW cm^{-2} sr^{-1}
Soil-emitted spectral radiance	$L_{i\ soil}$	mW cm^{-2} sr^{-1}
Sensor head-emitted spectral radiance	$L_{i\ head}$	mW cm^{-2} sr^{-1}
Reference standard-emitted spectral radiance	$L_{i\ RS}$	mW cm^{-2} sr^{-1}
Target emitted/reflected spectral radiance	$L_{i\ target}$	mW cm^{-2} sr^{-1}
Apparent soil-emitted spectral radiance	$L_{i'soil}$	mW cm^{-2} sr^{-1}
Target emitted/reflected radiance	L_{target}	mW cm^{-2} sr^{-1}
Maximum-minimum difference (TES algorithm)	MMD	(−)
One of five sensor-specific empirical constants	n_i	(−)
Relative humidity	RH	(−)
Radiometric sensitivity of channel i	S_i	(−)
Temperature	T	K
Apparent soil surface temperature	T'_{soil}	K
Air temperature	T_{air}	°C
Blackbody temperature	T_{BB}	K
Sensor head temperature used to calibrate S_i	T_{cal}	K
Sensor head temperature	T_{head}	K
Target brightness temperature	$T_{i\ target}$	K
Apparent soil brightness temperature	$T_{i'soil}$	K
Temperature/emissivity separation algorithm	TES	
Optimization factor	α_i	K^2
Ratio between soil and target radiances (TES algorithm)	β_i	(−)
Bandwidth	Δ_i	μm
Emissivity	ε	(−)
Apparent emissivity	ε'	(−)
Emissivity for channel i	ε_i	(−)
Reference standard emissivity for channel i	$\varepsilon_{i\ RS}$	(−)
Minimum emissivity (TES algorithm)	ε_{min}	(−)
Reference waveband emissivity	ε_{ref}	(−)
Wavelength	λ	μm
Air transmittance (between the sensor and the target)	τ_{air}	(−)
Sensor filter transmittance	τ_i	(−)

a combination of the radiation reflected or emitted by the target, and by the air between the sensor and the target:

$$L_{detected} = L_{target}\tau_{air} + L_{air} \tag{1}$$

where L_{target} and L_{air} are target and air radiances, respectively, and τ_{air} is the transmittance of the air between the sensor and the target. As in this study the distance between the target and the sensor was small (≤ 0.5 m), it was assumed that $L_{air} = 0$ and $\tau_{air} = 1$ so that $L_{detected} = L_{target}$.

3.1. Target brightness temperature

Following Sicard et al. (1999) and Legrand et al. (2000), for a blackbody surface, the spectral radiance (L_i) reaching the sensor detector on channel i for a given wavelength (λ) across bandwidth Δ_i, is the product of the Planck blackbody spectral radiance (B) of the surface, and the transmittance of the sensor filter (τ_i), so that:

$$L_i(T) = \int_{\Delta_i\lambda} B_\lambda(T)\tau_i(\lambda)d\lambda \tag{2}$$

where T is the blackbody temperature. $L_i(T)$ can be approximated by an empirical equation:

where a_i, b_i, n_i, and d_i are sensor-specific empirical constants (Legrand et al., 2000).

$$L_i(T) = \frac{a_i}{exp\left(\frac{b_i}{T^{n_i}}\right) - d_i} \tag{3}$$

Each target surface measurement requires a measurement of the internal radiation of the sensor head which is obtained using a retractable mirror. The sensor detector output in digital counts (DC) for the target and the mirror are proportional to the spectral radiance coming from the target ($L_{i\ target}$) and the sensor head ($L_{i\ head}$), so that:

$$S_i = \frac{DC_{i\ target} - DC_{i\ head}}{L_{i\ target} - L_{i\ head}} \tag{4}$$

where S_i is the radiometric sensitivity of channel i and $L_{i\ head}$ is obtained with Eq. (3) using T_{head} measured by a calibrated platinum probe inside the sensor head. Finally, temperature dependence of S_i on T_{head} is calculated as:

$$S_i(T_{head}) = S_i(T_{cal})exp(e_i \times (T_{head} - T_{cal})) \tag{5}$$

where T_{cal} is the head temperature for which S_i was calibrated and e_i is a sensor-specific empirical constant. Given Eqs. (3)–(5):

$$L_{i\ target} = \frac{DC_{i\ target} - DC_{i\ head}}{S_i\ exp(e_i \times (T_{head} - T_{cal}))} + \frac{a_i}{exp(T_{head}^{n_i}) - d_i} \tag{6}$$

Target brightness temperature ($T_{i\ target}$) for channel i, which for a blackbody is the same as the kinetic target temperature (T_{target}), is then obtained by inverting Eq. (3):

$$T_{i\ target} = \left(\frac{b_i}{log\left(\frac{a_i}{L_{i\ target}} + d_i\right)}\right)^{\frac{1}{n_i}} \tag{7}$$

3.2. Surface emissivity

When the target surface is a soil, measured $L_{i\ target}$ is a composite of the radiation emitted by the soil and radiation emitted from the sky and reflected by the soil:

$$L_{i\ target} = \varepsilon_i L_{i\ soil} + (1 - \varepsilon_i)L_{i\ sky} \tag{8}$$

where $L_{i\ soil}$ and $L_{i\ sky}$ are the spectral radiances from the soil and the sky, respectively, and ε_i is the soil surface emissivity for channel i. This equation can be rewritten to determine ε_i, the variable of interest in this paper:

$$\varepsilon_i = \frac{L_{i\ target} - L_{i\ sky}}{L_{i\ soil} - L_{i\ sky}} \tag{9}$$

where $L_{i\ sky}$ and $L_{i\ soil}$ are the two unknown variables. $L_{i\ sky}$ can be obtained by measuring $L_{i\ target}$ over a highly reflective reference standard:

$$L_{i\ sky} = \frac{L_{i\ target} - \varepsilon_{i\ RS}L_{i\ RS}}{(1 - \varepsilon_{i\ RS})} \tag{10}$$

where reference standard ε_i ($\varepsilon_{i\ RS}$) is known, and the spectral radiance of the reference standard itself ($L_{i\ RS}$) can be derived from Eq. (3) using the measured kinetic temperature of the reference surface.

3.3. Apparent soil surface emissivity

Computing $L_{i\ \text{soil}}$ requires knowledge of the kinetic temperature of the soil surface, but this is very challenging to measure. Therefore, apparent (or relative) emissivity (ε') is commonly used as a proxy for ε (Gillespie et al., 1998, 2011), where one or more channels serve as a reference for the other channels. Here we tested two approaches to determine ε', a single reference band and the TES:

— Single reference band approach (1B)

A fixed value for ε is used for the reference waveband (ε_{ref}) to infer the apparent kinetic soil surface temperature (T'_{soil}):

$$T'_{\text{soil}} = \left(\frac{b_{ref}}{log\left(\frac{\varepsilon_{ref} a_{ref}}{L_{ref\ \text{target}} - \left(1 - \varepsilon_{ref} \right) L_{ref\ \text{sky}}} + d_{ref} \right)} \right)^{\frac{1}{n_{ref}}} \quad (11)$$

as can be derived by bringing Eq. (8) into Eq. (7). Apparent $L_{i\ \text{soil}}$ ($L_i'_{\text{soil}}$) as a function of T'_{soil} (Eq. (3)), is then used to determine ε_i' (Eq. (9)).

Initial assessment of emissivity indicated that soil brightness temperatures measured for the 11.35 μm band were consistently higher than in all other bands, followed by the brightness temperatures measured for the 10.65 μm band. This is consistent with results reported by Mira et al. (2010). The remaining three bands had much lower brightness temperatures. Soil surface emissivity was therefore calculated using the 11.35 μm band as the reference waveband. ε_{ref} for the 11.35 μm band was set to 1 to minimize errors due to the highly variable $L_{i\ \text{sky}}$. Since $L_{i\ \text{sky}}$ measurements were found to be much more variable than $L_{i\ \text{target}}$, and therefore prone to error, any reduction in ε_{ref} ($\varepsilon_{ref} < 1$), greatly increased the variability in calculated ε_i' values, making it hard to determine patterns.

— the temperature/emissivity separation approach (TES)

In the TES algorithm (Gillespie et al., 2011), rather than using a single reference channel, individual channels are ratioed to the average of all channels as follows: an initial T'_{soil} is computed using the channel that can provide the largest initial value as the reference channel (Eq. (11), $\varepsilon_{ref} = 0.97$, $L_{ref\ \text{sky}}$ from Eq. (10)). Initial $L_i'_{\text{soil}}$ for each channel is then calculated as a function T'_{soil} using Eq. (3). The ratio of $L_{i\ \text{target}}$ and $L_i'_{\text{soil}}$ and average $L_{i\ \text{target}}$ and $L_i'_{\text{soil}}$ for all channels is given as:

$$\beta_i = \frac{L_{i\ \text{target}} \overline{L_i'_{\text{soil}}}}{L_i'_{\text{soil}} \overline{L_{i\ \text{target}}}} \quad (12)$$

After calculating β_i for each channel, the maximum-minimum difference (MMD = max(β_i) – min(β_i)) is used to determine minimum emissivity (ε_{min}) and ε_i':

$$\varepsilon_{min} = 0.994 - 0.667\text{MMD}^{0.737} \quad (13)$$

$$\varepsilon_i' = \beta_i \left(\frac{\varepsilon_{min}}{min(\beta_i)} \right) \quad (14)$$

where the relationship between ε_{min} and MMD was developed using emissivity data of minerals, soils, vegetation, and water (Nerry et al., 1996; Salisbury and D'Aria, 1992) in (Schmugge et al., 1998). Apparent $T_{i\ \text{soil}}$ ($T_i'_{\text{soil}}$) is then calculated for each channel (Eq. (11), $\varepsilon_{ref} = \varepsilon_i'$), and the average $T_i'_{\text{soil}}$ for all channels becomes the new T'_{soil}. The calculation of ε_i' is repeated until there is no change in T'_{soil} (Differences <0.001 generally within 12 iterations).

3.4. Calibration procedure

The calibration coefficients required to calculate L_i and T_i include five parameters that are independent of the radiometer head temperature (T_{head}); a_i, b_i, n_i, d_i, and S_i, and one parameter e_i that modifies S_i as a function of T_{head} (Eq. (5)). To calibrate a_i, b_i, n_i, d_i, and S_i, instead of keeping the head temperature at a fixed temperature, which proved very difficult to do at higher target temperatures as the radiometer head would warm up, we opted to keep the target temperature constant while allowing the head temperature to change. The calibration data was then filtered to only include datapoints for which T_{head} was within a quarter degree of 22 °C. Note that T_{cal} was 22 °C, rather than the conventional 21 °C, since for target temperatures of 60 °C T_{head} never reached 21 °C. This resulted in 26 datapoints (7, 9, and 10 datapoints for target temperatures of 10 °C, 35 °C, and 60 °C, respectively) for each bandwidth. For each of the target temperatures, the average difference between T_{BB} and T_i was determined. The sum of the squares of these three values provided a single value (α_i) representing the degree to which the brightness temperature for a particular bandwidth approached blackbody temperature. The calibration coefficients were optimized using the Solver function in Microsoft Excel, which uses a generalized reduced gradient (GRG) non-linear optimization algorithm to obtain a locally optimal solution. Solver was set up to adjust a_i, b_i, n_i, d_i, and S_i to minimize α_i, using factory calibration values as a starting point. Solving for one individual parameter at the time gave similar solutions to solving for all parameters at once, so a_i, b_i, n_i, d_i, and S_i were scaled and then optimized using a single optimization. This procedure was repeated for all six bandwidths.

Following the calibration of a_i, b_i, n_i, d_i, and S_i, the whole calibration dataset, for which T_{head} ranged between 17 °C and 46 °C, was used to calibrate for e_i. Since the factory did not supply calibration coefficients for e_i, $e_i = 0$ was used as the initial estimate in the optimization procedure. First, the sum of squares of the difference between T_{BB} and T_i was determined for the whole data set. Subsequently, Solver was used to minimize this value by adjusting e_i.

4. Results and discussion

4.1. Radiometer calibration

Using the factory calibration, the band-specific average difference between the blackbody and the sensor's measured brightness temperatures for the different bands at $T_{\text{head}} = 22 \pm 0.25$ °C ranged from 0.3 to 0.8 °C for $T_{\text{BB}} = 10$ °C and $T_{\text{BB}} = 35$ °C. For $T_{\text{BB}} = 60$ °C, which is outside the range of the factory calibration, differences were 0.6–1.9 °C. Optimization of a_i, b_i, n_i, d_i, and S_i reduced these differences to 0.002–0.025 °C.

Relative to the factory calibration coefficients, study-specific calibration coefficients showed a 1–3% increase in a, 2–5% increase in b, $<1\%$ increase in n, virtually no change in d, and an increase in S of up to 2% for all bands except the 11.35 μm band. The 11.35 μm band had a much lower increase in a of 0.3%, and much larger increases in b (13%), n (3%), d (15%), and S (2%). This is likely an artifact of the optimization procedure, and appears to have no bearing on the improved accuracy of ε, which is similar for all bands (Fig. 3). Calibrated e_i was -0.00015 for the 9.1 μm band, and ranged between 0.0004 and 0.0011 for the other bands.

Since the objective of this study was to use the radiometer to determine ε, ε_i rather than the absolute temperature difference between T_{BB} and T_i is shown in Fig. 3 to assess the level of accuracy that can be achieved with the different calibration coefficients. Factory calibration coefficients resulted in ε_i values within 0.005–0.035 of 1 (Fig. 3A), equivalent to $|T_{\text{BB}} - T_i| \le 2.5$ °C, while calibration of a_i, b_i, n_i, d_i, and S_i improved ε_i values within <0.01 of 1 (Fig. 3C), equivalent to $|T_{\text{BB}} - T_i| \le 0.7$ °C. Accounting for changes in T_{head} further improved ε_i values to within <0.003 of 1 (Fig. 3E), equivalent to $|T_{\text{BB}} - T_i| \le 0.2$ °C. Note that, under field conditions, it is unlikely that T_{head} would reach 40 °C or more at a time when the soil surface temperature approaches 10 °C, or, vice versa, that T_{head} would be as low as 22 °C when the soil surface
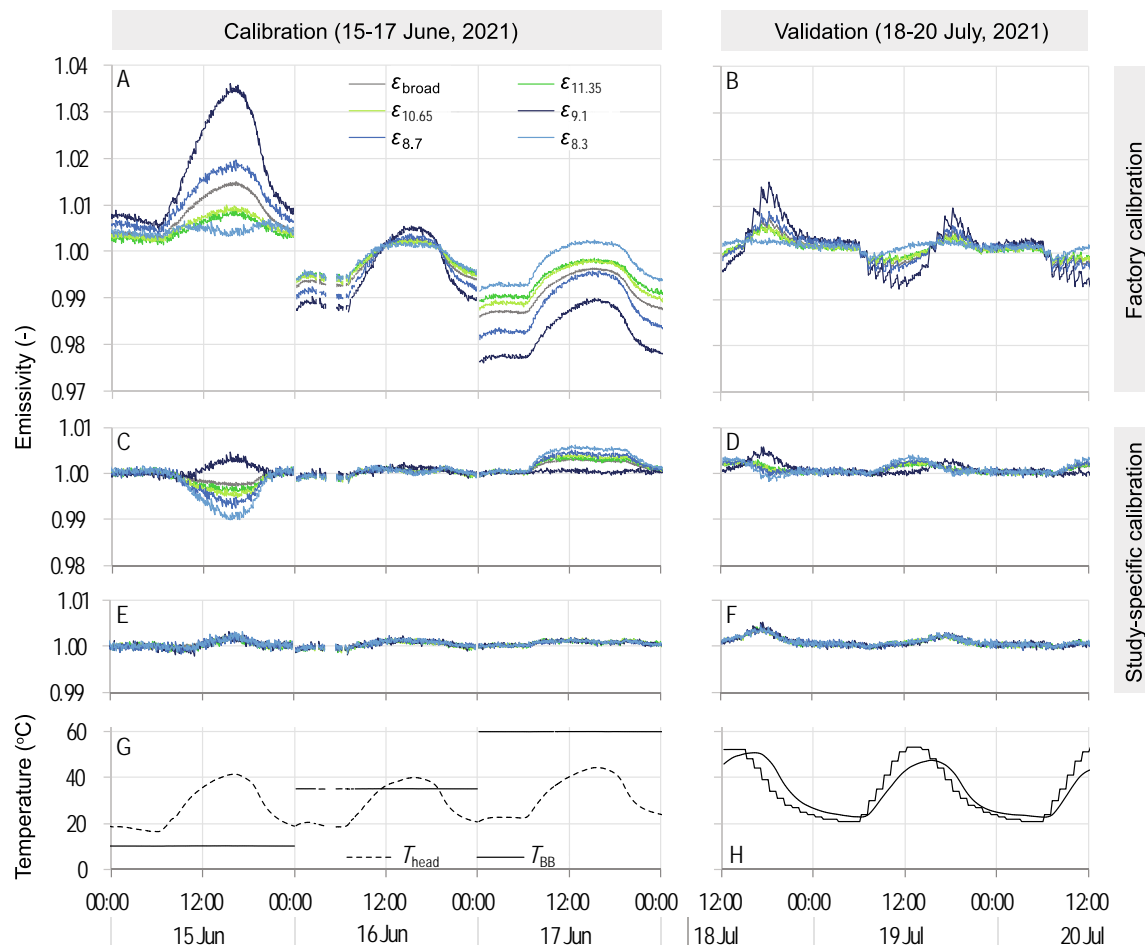
Fig. 3. Spectral emissivity (ε_i) for each channel i: the broad band (i = broad), and the 11.35 μm, 10.65 μm, 9.1 μm, 8.7 μm, and 8.3 μm bands, respectively, (i = respective band number) (A-F) along with the temperatures of the radiometer head (T_{head}) and the blackbody (T_{BB}) (G-H). Calculated ε_i using factory calibration coefficients (A-B), is compared to study-specific calibration coefficients (C—D), and study-specific calibration coefficients that also account for T_{head} (E-F).

temperature approaches 60 °C. For the validation period the blackbody temperature was similar to temperatures that could be expected under field conditions (Fig. 3H). Under these conditions, the factory calibration values could estimate ε_i within an accuracy of 0.015 (Fig. 3B), equivalent to $|T_{BB} - T_i| \leq 1.2\,°C$, while the full study-specific calibration could estimate ε_i within an accuracy of 0.005 (Fig. 3F), equivalent to $|T_{BB} - T_i| \leq 0.4\,°C$. The study-specific recalibration of the radiometer, aimed to observe ε changes with very small changes in soil water contents under very dry conditions, greatly improved the accuracy of ε'.

4.2. Detecting water vapor adsorption

4.2.1. Meteorological conditions

Weather data for a representative week (Fig. 4) showed typical summertime conditions, with mostly cloudless days and little day-to-day variation. Cloudy conditions occurred on the morning of 3 September, as can be observed from the reduction in incoming shortwave irradiance ($I_{S\downarrow}$), as well as from a corresponding sudden increase in incoming longwave irradiance ($I_{L\downarrow}$) (Fig. 4A). Sudden increases in $I_{L\downarrow}$ during the night indicate that cloudy conditions were more common in the early morning hours before sunrise than during the day. Air temperature ranged between 20 °C and 35 °C, while soil surface brightness temperature, as measured for the 11.35 μm band over the sand sample, ranged between 17 °C and 50 °C. The largest gradient in temperature between the soil and the air occurred around noon, with a temperature difference of at least 15 °C. The relative humidity was minimal (~30%) around 14:00, after which it started increasing, reaching about 90% around 6:00

on most nights, decreasing thereafter. North-westerly winds peaked around 16:00 in the afternoon, reaching maximum speeds of 6–8 m s^{-1}. These winds are generally associated with the sea breeze which brings in moist air from the Mediterranean Sea.

4.2.2. Determining emissivity

Similar to the measured $I_{L\downarrow}$, $L_{8.3sky}$ showed sharp increases in response to cloudy conditions (Fig. 5). This can also be observed in $L_{8.3target}$, which is a composite of the sky and the soil. The third radiance component, $L'_{8.3soil}$, derived from the 11.35 μm band measurement ($T'_{soil} = T_{11.35target}$), shows small increases in response to clouds as well. Since the $I_{S\downarrow}$ at night is zero, the net effect of cloudy conditions at night is an increase in net irradiance at the soil surface, and it is not uncommon to see soil temperatures increase during the night when cloudy conditions occur. However, the fact that ε_{ref} was set to 1, means that the contribution of $L_{11.35sky}$ to $L_{11.35target}$ is not accounted for, and that derived $L'_{8.3soil}$ may at times reflect changes in the sky rather than in the soil.

Since $L_{i\,sky}$ and $L_{i\,target}$ could not be measured simultaneously, large variability in $L_{i\,sky}$ during cloudy conditions introduced noise into calculated $\varepsilon_{8.3}'$ (Fig. 5). However, since $L_{i\,sky}$ measurements were conducted both before and after each $L_{i\,target}$ measurement, the difference between these two $L_{i\,sky}$ measurements could be used as an indicator of the variability in $L_{i\,sky}$ during $L_{i\,target}$ measurements. The resulting uncertainty in $\varepsilon_{8.3}'$ could be quantified by calculating $\varepsilon_{8.3}'$ using only the first $L_{i\,sky}$ measurement, recalculating $\varepsilon_{8.3}'$ using only the second $L_{i\,sky}$ measurement, and comparing the two values for $\varepsilon_{8.3}'$. In order to observe
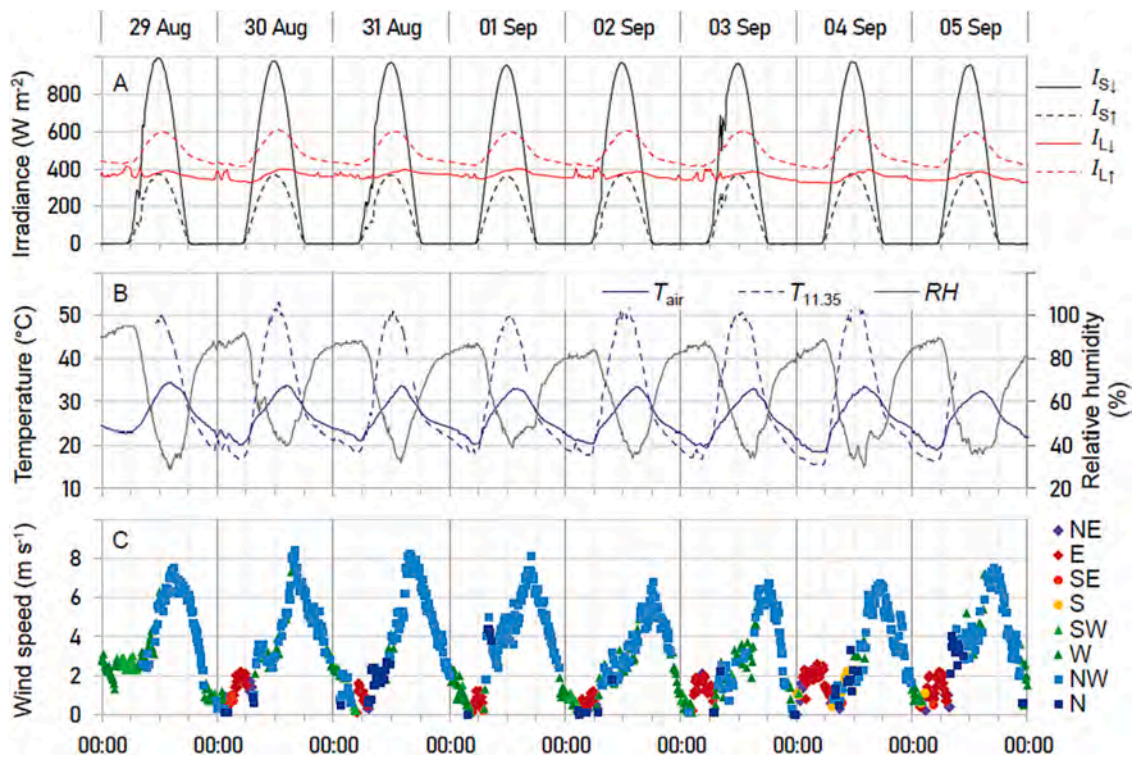
Fig. 4. Site conditions for a representative summer week (29 August to 5 September 2021) at Mashash experimental station, including: incoming (↓) and outgoing (↑) shortwave (I_S) and longwave (I_L) irradiance at 3 m height (A); air temperature (T_{air}) and relative humidity (*RH*) at 2 m height along with soil surface brightness temperature in the 11.35 μm band ($T_{11.35}$) (B); wind speed at 10 m height, color-coded to indicate wind direction: north-east (NE), east (E), south-east (SE), south (S), south-west (SW), west (W), north-west (NW), and north (N) (C).
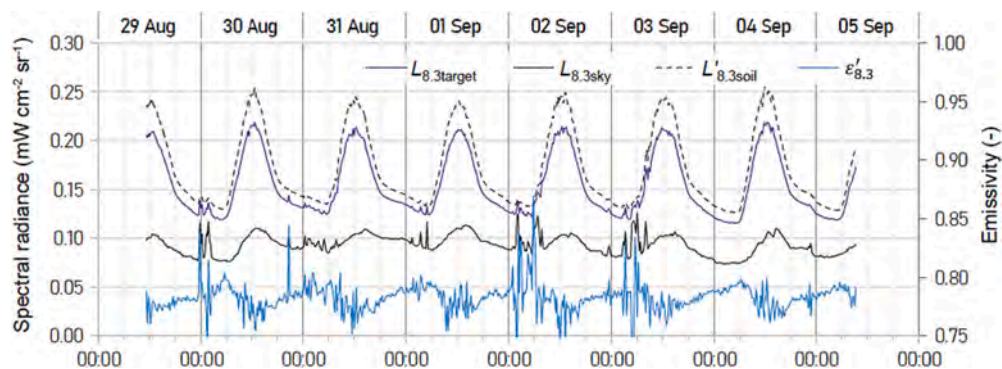

Fig. 5. Spectral radiance target ($L_{i\ target}$) and sky ($L_{i\ sky}$) measurements for the 8.3 μm band ($i = 8.3$), as well as the apparent spectral soil radiance ($L_{i\ soil}'$), with resulting spectral soil surface emissivity (ε_i') over sand (29 August to 5 September 2021).

diurnal changes ranging between 0.77 and 0.80, the threshold for reliable data was set to 0.001, meaning that the two values for $\varepsilon_{8.3}'$ should be <0.001 apart.

This filtering approach reduced uncertainty in $\varepsilon_{8.3}'$ during cloudy conditions, but, as can be observed in Fig. 5, scatter in calculated $\varepsilon_{8.3}'$ also appeared to be high around noon, unrelated to variability in $L_{i\ sky}$. Several reasons could be considered. High wind speeds might cause the radiometer arm to shake, disturbing the measurements. This appears to be unlikely, given that windspeeds were highest between 15:00 and 18:00 in the afternoon (Fig. 4C), and around 18:00 the scatter in $\varepsilon_{8.3}'$ is minimal. Another reason could be that around noon the temperature gradient between the soil and the air is very large, which means that the slightest wind gust may cause large changes in soil surface temperature. Given that the 8.3 and 11.35 μm bands were measured consecutively rather than simultaneously, this may have introduced additional uncertainty into the measurement. Unfortunately, since measurements of

the 11.35 μm band were only conducted once during each measurement sequence, this variability could not be quantified. However, 2-hourly averages helped reveal the diurnal pattern that may have been obscured by the scatter (Fig. 6).

4.2.3. Comparing emissivity calculation approaches

The diurnal pattern of water accumulation due to water vapor adsorption and evaporation was similar in both soils (Fig. 6). Lysimeter-measured water content showed a clear diurnal pattern; the increase in water content started at about 16:00, continuing through the night until 6:00 in the morning of the following day. The initiation of water accumulation coincided with maximum wind speeds bringing in the sea breeze (Fig. 4C) and totaled about 0.4 mm per night. Similarly, $\varepsilon_{8.3}'$ was observed to increase over the course of the night, which can be attributed to increases in water content. Water accumulation in loess was larger, totaling about 0.6 mm per night. This was expected, since loess
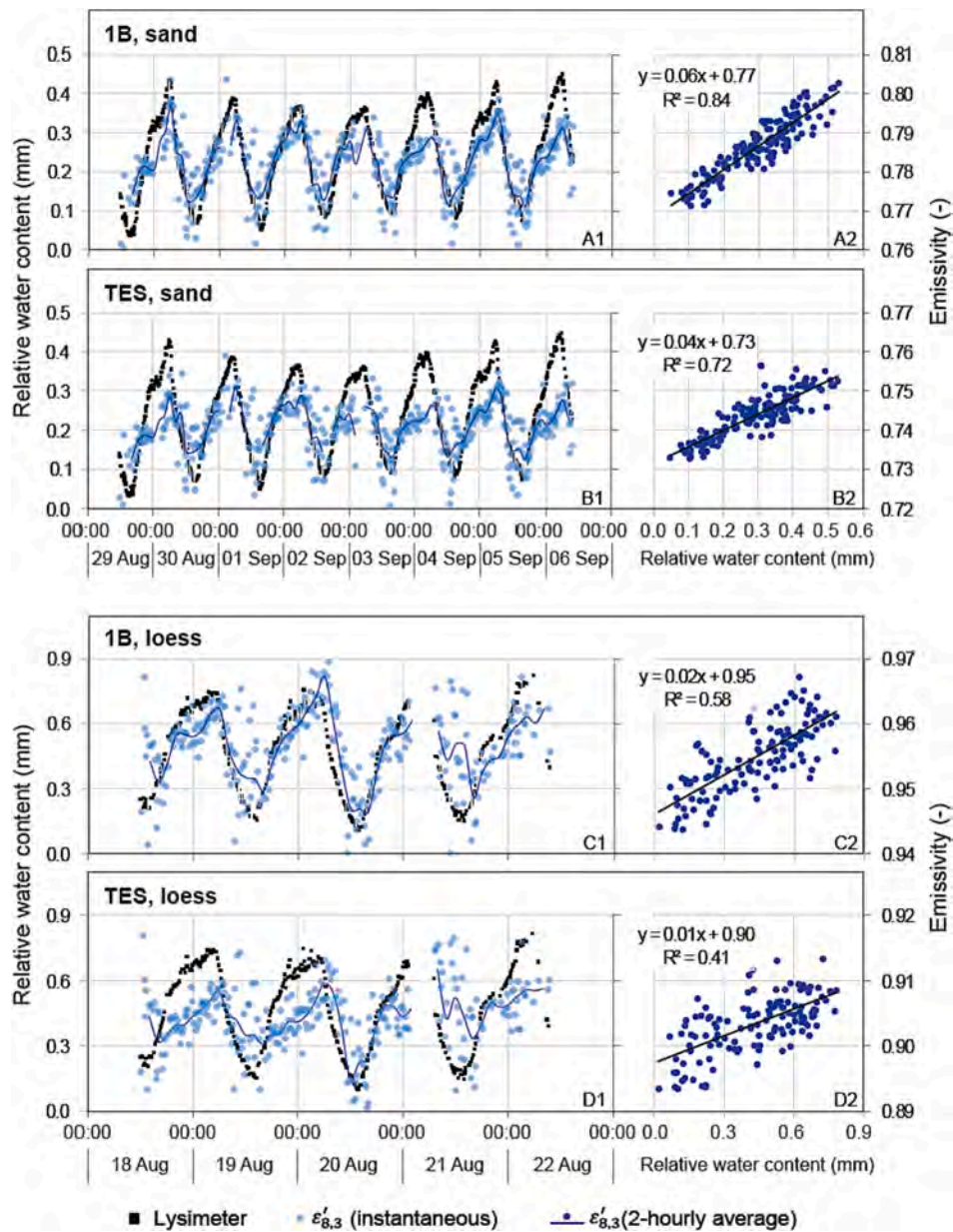
Fig. 6. Comparison of lysimeter-measured diurnal changes in water content and diurnal changes in apparent soil surface emissivity for the 8.3 μm band ($\varepsilon_{8.3}'$) for sand (A and B) and loess (C and D), derived using the single reference band (1B; A and C) and the temperature/emissivity separation approach (TES; B and D). Measurements were conducted in 2021 between 29 August - 5 September (sand) and between 18 and 22 August (loess). Scatterplots also include data collected between 12 and 19 September (sand; A2, B2) and 26–29 August and 19–23 September (loess; C2, D2). Measurements were conducted at 15-min intervals (sand: $n = 1003$, loess: $n = 749$), and averaged to 2-hourly values (sand: $n = 158$, loess: $n = 124$).

has finer textured soil particles than sand, and therefore more surface area for water molecules to adsorb to. Both the TES and the 1B approaches could pick up on the diurnal changes in water content observed in the lysimeters.

Generally, $\varepsilon_{8.3}'$ followed the lysimeter diurnal pattern in sand better than in loess. In sand, the 1B had a slightly better correlation than the TES ($R^2 = 0.84$ vs. 0.72, Fig. 6A2 and 6B2), while in loess the difference between the approaches was larger ($R^2 = 0.58$ vs. 0.41, Fig. 6C2 and 6D2). The range of $\varepsilon_{8.3}'$ values was similar for both loess and sand (~0.02) even though the changes in water content were much greater in loess (~0.65 vs. ~0.35 mm, respectively, Fig. 6). This means that the changes in emissivity are more sensitive to changes in water content in sand, explaining the better correlation. The similar range in $\varepsilon_{8.3}'$ over loess, despite having a larger range in water content, might have more than one explanation. The dry cracked structure of the surface of the

loess sample (Fig. 2) could decrease the spectral contrast, as has been observed in a dry soil in central Arizona (Sanchez et al., 2011). The spectral properties of the soil minerals and organic matter may also contribute to the different spectral response observed in sand and loess. The TES approach uses the average of all bands rather than one particular band as a reference, perhaps this made for a less clear contrast in emissivity in this particular case. Another explanation for the better performance of the 1B method might be that the reference emissivity (ε_{ref}) was set to 1, reducing the error introduced by variability in $L_{i\,sky}$ (see Section 3.3). TES on the other hand, uses a fixed emissivity of 0.97 for its reference.

4.3. Possible use of other spectral bands

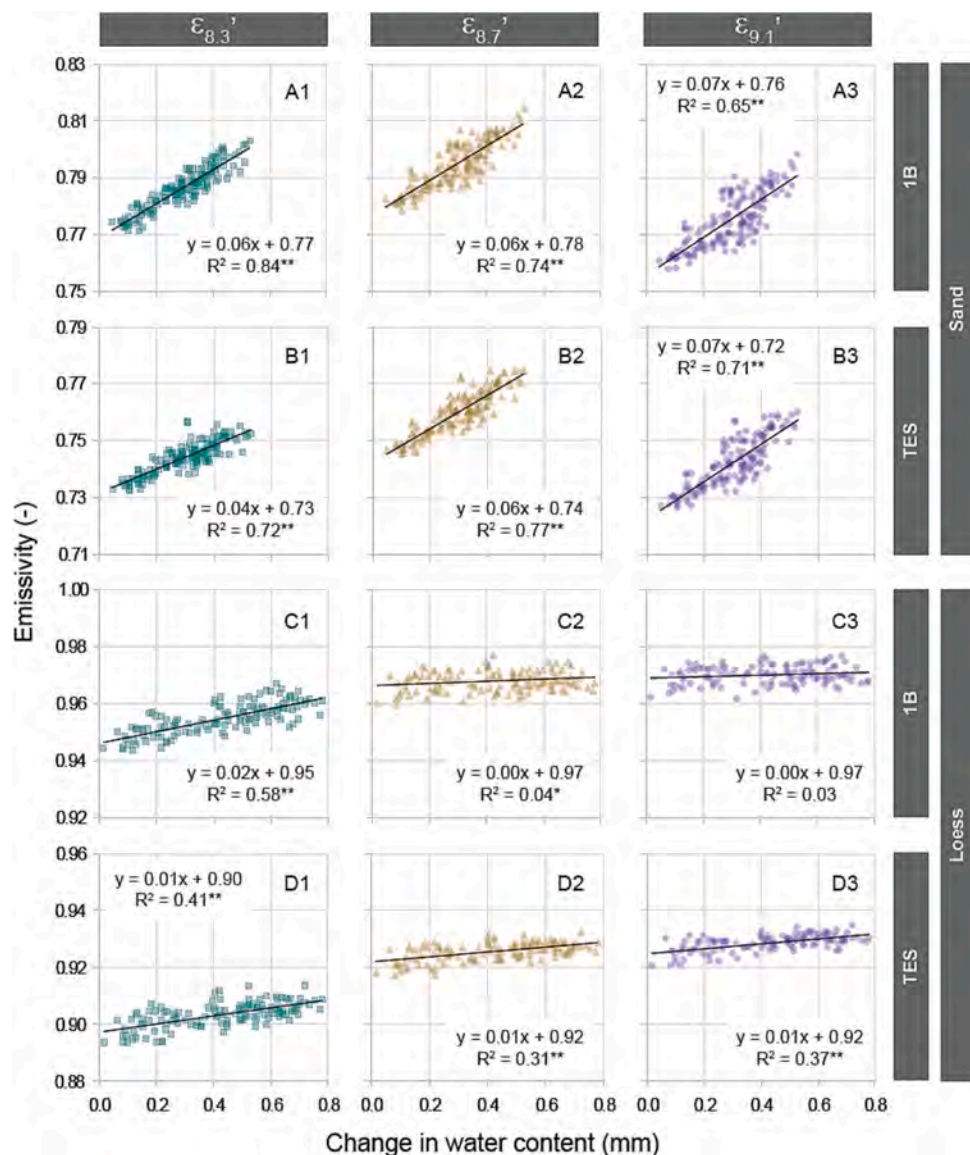Calculations described above for the 8.3 μm band were also

Fig. 7. Comparison of lysimeter-measured diurnal changes in water content and diurnal changes in apparent soil surface emissivity for the 8.3, 8.7 and 9.1 μm bands ($\varepsilon_{8.3}'$, $\varepsilon_{8.7}'$, $\varepsilon_{9.1}'$) for sand (A and B) and loess (C and D), derived using the single reference band (1B; A and C) and the temperature/emissivity separation approach (TES; B and D). Measurements were conducted in 2021 between 29 August - 9 September (sand) and between 18 August - 23 September (loess). Measurements were conducted at 15-min intervals and averaged to 2-hourly values (sand: $n = 158$, loess: $n = 124$).

performed for the 8.7 μm and 9.1 μm bands (Fig. 7). For sand, vapor adsorption-derived changes in soil water content resulted in relatively large changes in ε' in all three bands, where a gain of 1 mm in soil water content corresponded to an increase of 0.060–0.067 in ε' for 1B (Fig. 7A) and to an increase of 0.042–0.065 in ε' for TES (Fig. 7B). The differences between the channels were small, indicating that for sand any of the three channels can be used to detect water content changes due to water vapor adsorption, with the 1B approach slightly outperforming the TES.

The response of ε' to changes in soil water content were an order of magnitude smaller in loess, albeit changes in water content were larger, thus the slope was significantly smaller (a gain of 1 mm in soil water content corresponded to an increase of 0.003–0.020 in ε' for 1B (Fig. 7C) and to an increase of 0.009–0.014 in ε' for TES (Fig. 7D). This explains why the R^2 in loess is much lower than in sand. As opposed to sand, in loess there were distinct differences between the three bands, with the 8.3 μm clearly outperforming the other two in both approaches. The 1B again outperformed the TES. Overall, for both soils, best results were obtained using the 1B approach with the 8.3 μm band.

5. Remaining challenges and future applications

Diurnal changes in emissivity, observed over desert regions, have been associated with water vapor adsorption for some time (Li et al., 2012; Masiello et al., 2013, 2014; Mushkin et al., 2020; Rozenstein et al., 2015), but this is the first time that we were able to conclusively show changes in emissivity with concurrent measurements of water vapor adsorption-induced changes in soil water content. The day-night differences in soil water content imply that in arid regions, caution is advised when comparing remotely sensed data collected at different times of the day. However, to accurately upscale emissivity derived soil water contents, several remaining challenges must first be addressed:

— Air radiance

Radiance detected by the radiometer is a combination of the radiation reflected (L_{sky}) or emitted (L_{soil}) by the target, and by the air between the sensor and the target (L_{air}). The diurnal change in L_{sky} was ~0.025 mW cm^{-2} sr^{-1} versus, for example, ~0.125 mW cm^{-2} sr^{-1} for

$L'_{8.3soil}$ over sand (Fig. 5). In this study L_{air} could be ignored because of the proximity of the radiometer to the soil surface (~0.5 m). Assuming that for large distances between the radiometer and the soil surface, L_{air} is affected by water vapor in a similar way as L_{sky}, L_{air} can no longer be ignored. Preventing L_{air} from obscuring the surface processes is a major challenge in upscaling this method to airborne and certainly spaceborne applications.

— Surface heterogeneity

A second challenge for spatially upscaling this method is to separate between soil- and plant-related processes, especially given the spatial resolution of existing satellite thermal products. Unless the effect of vegetation is satisfactorily determined, detecting changes in water content due to water vapor adsorption will only be possible where large areas are completely barren.

— Soil spectral properties

This work shows that for both coarse and finer-textured soils, emissivity can be used as an indicator of soil water content changes due to water vapor adsorption and subsequent evaporation. This concurs with what has been found by a range of studies: that coarser soils tend to have lower emissivities and higher sensitivity to changes in water content (Mira, 2007; Mira et al., 2010; Salisbury and D'Aria, 1992; Wang et al., 2015). Additional work on the spectral properties of various soil types, particularly for the dry end (<0.05 cm^3 cm^{-3}) will be needed before water vapor adsorption-induced soil water content can be detected at large scales.

Meeting these main challenges will lead the way to detect small changes in soil water content under dry conditions at larger scales. Whether these are a result of water vapor adsorption or other processes, detecting such small changes in soil water content will provide new insights into desert hydrology.

CRediT authorship contribution statement

D. Kool: Conceptualization, Data curation, Formal analysis, Investigation, Methodology, Validation, Visualization, Writing – original draft, Writing – review & editing. **N. Agam:** Conceptualization, Funding acquisition, Project administration, Resources, Writing – review & editing.

Declaration of competing interest

The authors declare that they have no known competing financial interests or personal relationships that could have appeared to influence the work reported in this paper.

Data availability

Data will be made available on request.

Acknowledgment

References

Agam, N., Berliner, P.R., 2004. Diurnal water content changes in the bare soil of a coastal desert. J. Hydrometeorol. 5, 922–933. https://doi.org/10.1175/1525-7541(2004)005<0922:DWCCIT>2.0.CO;2.

Agam, N., Berliner, P.R., Zangvil, A., Ben-Dor, E., 2004a. Soil water evaporation during the dry season in an arid zone. J. Geophys. Res. 109, D16103. https://doi.org/10.1029/2004JD004802.

Agam, N., Berliner, P.R., Zangvil, A., Ben-Dor, E., 2004b. Soil water evaporation during the dry season in an arid zone. J. Geophys. Res. 109, D16103. https://doi.org/10.1029/2004JD004802.

Babaeian, E., Sadeghi, M., Jones, S.B., Montzka, C., Vereecken, H., Tuller, M., 2019. Ground, proximal, and satellite remote sensing of soil water content. Rev. Geophys. 57, 530–616. https://doi.org/10.1029/2018RG000618.

Brocca, L., Ciabatta, L., Massari, C., Camici, S., Tarpanelli, A., 2017. Soil water content for hydrological applications: open questions and new opportunities. Water 9, 140. https://doi.org/10.3390/w9020140.

Brogniez, G., Pietras, C., Legrand, M., Dubuisson, P., Haeffelin, M., 2003. A high-accuracy multiwavelength radiometer for in situ measurements in the thermal infrared. Part II: behavior in field experiments. J. Atmos. Ocean. Technol. 20, 1023–1033. https://doi.org/10.1175/1520-0426(2003)20<1023:AHMRFI>2.0.CO;2.

Dorigo, W.A., Gruber, A., De Jeu, R.A.M., Wagner, W., Stacke, T., Loew, A., Albergel, C., Brocca, L., Chung, D., Parinussa, R.M., Kidd, R., 2015. Evaluation of the ESA CCI soil water content product using ground-based observations. Remote Sens. Environ. 162, 380–395. https://doi.org/10.1016/j.rse.2014.07.023.

Florentin, A., Agam, N., 2017. Estimating non-rainfall-water-inputs-derived latent heat flux with turbulence-based methods. Agric. For. Meteorol. 247, 533–540. https://doi.org/10.1016/j.agrformet.2017.08.035.

García-Santos, V., Valor, E., Caselles, V., Ángeles Burgos, M., Coll, C., 2012. On the angular variation of thermal infrared emissivity of inorganic soils. J. Geophys. Res. 117 https://doi.org/10.1029/2012JD017931 n/a-n/a.

GCOS, 2011. Systematic observation requirements for satellite- based products for climate 2011 update: Supplemental details to the satellite-based component of the Implementation plan for the global observing system for climate in support of the UNFCCC (2010 update) (GCOS Rep. No. 154).

Gillespie, A., Rokugawa, S., Matsunaga, T., Cothern, J.S., Hook, S., Kahle, A.B., 1998. A temperature and emissivity separation algorithm for advanced spaceborne thermal emission and reflection radiometer (ASTER) images. IEEE Trans. Geosci. Remote Sens. 36, 1113–1126. https://doi.org/10.1109/36.700995.

Gillespie, A.R., Abbott, E.A., Gilson, L., Hulley, G., Jiménez-Muñoz, J.-C., Sobrino, J.A., 2011. Residual errors in ASTER temperature and emissivity standard products AST08 and AST05. Remote Sens. Environ. 115, 3681–3694. https://doi.org/10.1016/j.rse.2011.09.007.

Hu, L., Zhao, T.J., Ju, W.M., Peng, Z.Q., Shi, J.C., Rodríguez-Fernández, N.J., Wigneron, J.P., Cosh, M.H., Yang, K., Lu, H., Yao, P., 2023. A twenty-year dataset of soil water content and vegetation optical depth from AMSR-E/2 measurements using the multi-channel collaborative algorithm. Remote Sens. Environ. 2023 (292), 113595 https://doi.org/10.1016/j.rse.2023.113595.

IPCC, 2021. In: Masson-Delmotte, V., Zhai, P., Pirani, A., Connors, S.L., Péan, C., Berger, S., Caud, N., Chen, Y., Goldfarb, L., Gomis, M.I., Huang, M., Leitzell, K., Lonnoy, E., Matthews, J.B.R., Maycock, T.K., Waterfield, T., Yelekçi, O., Yu, R., Zhou, B. (Eds.), Climate Change 2021: The Physical Science Basis. Contribution of Working Group I to the Sixth Assessment Report of the Intergovernmental Panel on Climate Change. Cambridge University Press, Cambridge, United Kingdom and New York, NY, USA.

Kool, D., Agra, E., Drabkin, A., Duncan, A., Fendinat, P.P., Leduc, S., Lupovitch, G., Nambwandja, A.N., Ndilenga, N.S., Nguyễn Thị, T., Poodiack, B., Sagi, L., Shmuel, Y., Maggs-Kölling, G., Marais, E., Pinshow, B., Turner, J.S., Agam, N., 2021. The overlooked rainfall water input sibling of fog and dew: daily water vapor adsorption on a !Nara hummock in the Namib Sand Sea. J. Hydrol. 598, 126420 https://doi.org/10.1016/j.jhydrol.2021.126420.

Legrand, M., Pietras, C., Brogniez, G., Haeffelin, M., Abuhassan, N.K., Sicard, M., 2000. A high-accuracy multiwavelength radiometer for in situ measurements in the thermal infrared. Part I: characterization of the instrument. J. Atmos. Ocean. Technol. 17, 1203–1214. https://doi.org/10.1175/1520-0426(2000)017<1203:AHAMRF>2.0.CO;2.

Li, Z., Li, J., Li, Y., Zhang, Y., Schmit, T.J., Zhou, L., Goldberg, M.D., Menzel, W.P., 2012. Determining diurnal variations of land surface emissivity from geostationary satellites: emissivity diurnal variations. J. Geophys. Res. 117 https://doi.org/10.1029/2012JD018279 n/a-n/a.

Lv, S., Yijian, Z., Jun, W., Hong, Z., Zhongbo, S., 2018. Estimation of penetration depth from soil effective temperature in microwave radiometry. Remote Sens. 10, 519. https://doi.org/10.3390/rs10040519.

Maltese, A., Capodici, F., Ciraolo, G., La Loggia, G., 2013. Mapping soil water content under sparse vegetation and changeable sky conditions: comparison of two thermal inertia approaches. J. Appl. Remote. Sens. 7, 073548 https://doi.org/10.1117/1.JRS.7.073548.

Masiello, G., Serio, C., De Feis, I., Amoroso, M., Venafra, S., Trigo, I.F., Watts, P., 2013. Kalman filter physical retrieval of surface emissivity and temperature from geostationary infrared radiances. Atmos. Meas. Tech. 6, 3613–3634. https://doi.org/10.5194/amt-6-3613-2013.

Masiello, G., Serio, C., Venafra, S., DeFeis, I., Borbas, E.E., 2014. Diurnal variation in Sahara desert sand emissivity during the dry season from IASI observations: diurnal emissivity variation. J. Geophys. Res. Atmos. 119, 1626–1638. https://doi.org/10.1002/jgrd.50863.

Mira, 2007. Influence of the soil water content effect on the thermal infrared emissivity. Tethys 4. https://doi.org/10.3369/tethys.2007.4.01.

Mira, M., Valor, E., Caselles, V., Rubio, E., Coll, C., Galve, J.M., Niclos, R., Sanchez, J.M., Boluda, R., 2010. Soil water content effect on thermal infrared (8–13-μm) emissivity. IEEE Trans. Geosci. Remote Sens. 48, 2251–2260. https://doi.org/10.1109/TGRS.2009.2039143.

Mushkin, A., Gillespie, A.R., Abbott, E.A., Batbaatar, J., Hulley, G., Tan, H., Tratt, D.M., Buckland, N., 2020. Validation of ASTER emissivity retrieval using the Mako

airborne TIR imaging spectrometer at the Algodones dune field in Southern California, USA. Remote Sens. 12, 815. https://doi.org/10.3390/rs12050815.

Nerry, F., Stoll, M.P., Pion, J.C., 1996. Infrared spectro-radiometry. In: Kerr, Y.H., Mahkmara, H., Meunier, J.C., Valero, T. (Eds.), HAPEX SAHEL Ground Data Version 4, CD-ROM 3. HSIS LERTS/CNES/ORSTOM, MEDIAS-FRANCE, Toulouse, France.

Ochsner, T.E., Cosh, M.H., Cuenca, R.H., Dorigo, W.A., Draper, C.S., Hagimoto, Y., Kerr, Y.H., Larson, K.M., Njoku, E.G., Small, E.E., Zreda, M., 2013. State of the art in large-scale soil water content monitoring. Soil Sci. Soc. Am. J. 77, 1888–1919. https://doi.org/10.2136/sssaj2013.03.0093.

Petropoulos, G.P., Ireland, G., Barrett, B., 2015. Surface soil water content retrievals from remote sensing: current status, products & future trends. Phys. Chem. Earth Parts A/B/C 84, 36–56. https://doi.org/10.1016/j.pce.2015.02.009.

Rozenstein, O., Agam, N., Serio, C., Masiello, G., Venafra, S., Achal, S., Puckrin, E., Karnieli, A., 2015. Diurnal emissivity dynamics in bare versus biocrusted sand dunes. Sci. Total Environ. 506–507, 422–429. https://doi.org/10.1016/j.scitotenv.2014.11.035.

Salisbury, J.W., D'Aria, D.M., 1992. Infrared (8–14 gm) Remote Sensing of Soil Particle Size, 42, pp. 157–165.

Sanchez, J.M., French, A.N., Mira, M., Hunsaker, D.J., Thorp, K.R., Valor, E., Caselles, V., 2011. Thermal infrared emissivity dependence on soil water content in field conditions. IEEE Trans. Geosci. Remote Sens. 49 (11), 4652–4659. https://doi.org/10.1109/TGRS.2011.2142000.

Schmugge, T., Hook, S.J., Coll, C., 1998. Recovering surface temperature and emissivity from thermal infrared multispectral data. Remote Sens. Environ. 65, 121–131. https://doi.org/10.1016/S0034-4257(98)00023-6.

Sicard, M., Spyak, P.R., Brogniez, G., Legrand, M., Abuhassan, N.K., Pietras, C., Buis, J.-P., 1999. Thermal-infrared field radiometer for vicarious cross-calibration: characterization and comparisons with other field instruments. Opt. Eng. 38, 345–356. https://doi.org/10.1117/1.602094.

Spirig, R., Vogt, R., Larsen, J.A., Feigenwinter, C., Wicki, A., Franceschi, J., Parlow, E., Adler, B., Kalthoff, N., Cermak, J., Andersen, H., Fuchs, J., Bott, A., Hacker, M., Wagner, N., Maggs-Kölling, G., Wassenaar, T., Seely, M., 2019. Probing the fog life cycles in the Namib desert. Bull. Am. Meteorol. Soc. 100, 2491–2507. https://doi.org/10.1175/BAMS-D-18-0142.1.

Verstraeten, W.W., Veroustraete, F., van der Sande, C.J., Grootaers, I., Feyen, J., 2006. Soil water content retrieval using thermal inertia, determined with visible and thermal spaceborne data, validated for European forests. Remote Sens. Environ. 101, 299–314. https://doi.org/10.1016/j.rse.2005.12.016.

Wang, H., Xiao, Q., Li, H., Du, Y., Liu, Q., 2015. Investigating the impact of soil water content on thermal infrared emissivity using ASTER data. IEEE Geosci. Remote Sensing Lett. 12, 294–298. https://doi.org/10.1109/LGRS.2014.2336912.

Zhao, T., Shi, J., Entekhabi, D., Jackson, T.J., Hu, L., Peng, Z., Yao, P., Li, S., Kang, C.S., 2021. Retrievals of soil water content and vegetation optical depth using a multi-channel collaborative algorithm. Remote Sens. Environ. 257, 112321 https://doi.org/10.1016/j.rse.2021.112321.

Zomer, R.J., Xu, J., Trabucco, A., 2022. Version 3 of the global aridity index and potential evapotranspiration database. Sci. Data 9, 409. https://doi.org/10.1038/s41597-022-01493-1.